metals

MDPI

Article

Mechanical Properties of Double-Layer Riveted Aluminum Roofing Panels with Curved Surfaces

Ye Yuan [1], Qilin Zhang [1,*], Xiaoqun Luo [1], Lin Yuan [1], Shaoquan Zhang [2] and Hanbin Ge [2]

[1] College of Civil Engineering, Tongji University, Shanghai 200092, China; yuanyetj@tongji.edu.cn (Y.Y.); luoxiaoqun@tongji.edu.cn (X.L.); yuanlin@tongji.edu.cn (L.Y.)
[2] Department of Civil Engineering, Meijo University, Nagoya 4688502, Japan; 203443502@ccmailg.meijo-u.ac.jp (S.Z.); gehanbin@meijo-u.ac.jp (H.G.)
* Correspondence: zhangqilin@tongji.edu.cn

Abstract: In recent years, aluminum alloy has been increasingly used in building structures, becoming an important construction material for metal structures. Currently, aluminum alloy is commonly used in buildings as beam–column components, profiled roof panels, and door and window frames, among other forms. However, there is limited research on the mechanical properties of aluminum alloy roof panels with irregular curved surfaces. In this study, a full-scale curved double-layer anisotropic riveted aluminum alloy roof panel was subjected to a load test to analyze its deformation patterns and failure mechanisms. The results indicate that the load-bearing capacity of the roof panel meets the design requirements. During failure, neither the upper nor lower layers of the panel enter the plastic deformation stage, indicating sufficient safety redundancy. The failure mode observed is a ductile failure with noticeable deformation with the weak points of the component being the riveted connections of the stiffeners. A finite element model was established for numerical simulation and the results matched well with the experimental data. Finally, a theoretical calculation for the ultimate load-bearing capacity of the roof panel was derived, providing a reference for design purposes.

Keywords: aluminum roofing panel; connection failure; experimental study; numerical simulation; design method

Citation: Yuan, Y.; Zhang, Q.; Luo, X.; Yuan, L.; Zhang, S.; Ge, H. Mechanical Properties of Double-Layer Riveted Aluminum Roofing Panels with Curved Surfaces. *Metals* **2023**, *13*, 1452. https://doi.org/10.3390/met13081452

Academic Editors: Giuseppe Lacidogna and Yong Zhang

Received: 3 July 2023
Revised: 31 July 2023
Accepted: 10 August 2023
Published: 12 August 2023

1. Introduction

Aluminum alloy is a kind of lightweight and high-strength metal, its surface is covered with an oxide film that gives it a glossy appearance and excellent corrosion resistance which makes it particularly suitable for large-span spatial structures and tower structures [1,2]. With advancements in aluminum alloy manufacturing processes, its application in construction engineering has become increasingly widespread, with many buildings featuring aluminum alloy as the main load-bearing component [3,4]. Currently, the application of aluminum alloy in construction engineering is mainly seen in vertical load-bearing components such as beams and columns, bracing elements in space grid structures, various profiled panels used for roofing, and door and window frames for decorative enclosure structures [5]. However, its application in irregular curved surface roof panels is relatively limited. Aluminum alloy materials are easily extruded into shape and possess excellent processability, making them well-suited for curved roof structures and offering promising prospects for application and research value.

Existing research primarily focuses on the mechanical properties of various aluminum alloy profiles. Yuan [6–8] and others have studied the buckling behavior of T-section and H-section aluminum alloy columns as well as the shear mechanical properties of I-beams, providing a series of buckling curves for columns and shear envelope curves. For profiled aluminum alloy roof panels, including standing seam, trapezoidal, and corrugated forms, Okafor [9], Avci [10], and others have investigated their bending and shear mechanical properties; the effect of different types of stiffening ribs on the mechanical properties of roof panels was investigated. Wang [11] and others have examined the mechanical properties of profiled roof panels under high-temperature conditions while Alphonso [12], Song [13], Luo [14], and others have studied the influence of extreme conditions and impact loads on roof panels, such as unconventional winds and random floating object impact events. Apart from profiled panels, aluminum alloy roof panels are commonly used in the form of flat panels [15,16]. Ribbed stiffeners and structural members can effectively enhance the bending resistance of roof panels. Brando [17], Paik [18,19], and others have proposed various design methods for ribbed aluminum alloy panels; a series of schemes and regulations are proposed for the arrangement of stiffening ribs and structural elements of roof slabs. Zha [20], Li [21], Paik [22], Luca [23], and others have conducted experimental and numerical studies on the load-carrying capacity and buckling performance of ribbed aluminum alloy panels; the results show that the arrangement of stiffeners is very important for the load carrying capacity, deformation modes, and buckling performance of roof panels. Zhao [24] and others have also researched the buckling performance of aluminum alloy roof components with honeycomb stiffening. Regarding curved metal panel components, the current application is mainly focused on steel materials with most used as stiffened structural plates for the undersides of steel bridges [25–27]; primarily, investigations focus on their in-plane compressive buckling behavior [28]. The results show that the force performance of curved roof panels is somewhat different from that of large-span planar panels and the curved beam or arch effect embodied in some cases affects the overall mechanical performance of the panels.

In summary, existing research content mainly focuses on aluminum alloy section profiles and planar stiffened roof panels; regarding steel structures, there are some studies on steel curved roof panels but applications and research on curved aluminum alloy roof panels are very few. This study focuses on conducting mechanical experiments and numerical simulations on curved aluminum alloy roof panels to investigate their mechanical behavior under out-of-plane loads. The tested roof panel is curved in one direction and flat in the other direction, with the panel composed of two layers joined by rivets. The panel is reinforced with aluminum alloy stiffeners and stainless steel tie rods beneath. The chosen configuration and structure of this roof panel are representative and studying it can provide insights into the mechanical properties of similar curved aluminum alloy roof panels.

2. Experimental Studies

2.1. Specimen Design

In the model experiment, aluminum alloy panels with dimensions of 3 m × 3 m were used. Such specimens possess sufficient scale to reflect the load–deformation characteristics of large-area roof panels while also being modular and suitable for assembling into complex curved surface forms. This makes them universally applicable for the application of aluminum curved alloy roof panels. The specimens were assembled using aluminum alloy strips in two different directions: the upper layer strips were distributed to be parallel at a 45° angle while the lower layer strips were distributed horizontally. To better simulate the general state of aluminum curved alloy panels and seams were introduced at the middle positions of the two longest strips in the upper layer and at different locations in the lower layer. These seams divided the strips into different-sized and shaped assembly sections. The decomposition and numbering diagram of the upper and lower aluminum alloy panels are shown in Figure 1.

The aluminum alloy panels are divided into a 5 × 5 grid with grid dimensions of approximately 600 mm. The upper and lower layer strips are arranged in an intersecting pattern and they are connected using rivets. Within each grid, the minimum constituent element of the aluminum alloy panel is a plane unit in the shape of an equilateral right triangle. By continuously folding these triangular panels, the overall curved shape of the roof is formed. This construction not only allows the roof to take on various forms of freeform surfaces but also facilitates the manufacturing process. The double-layer panels can be effectively connected, enabling them to work together.

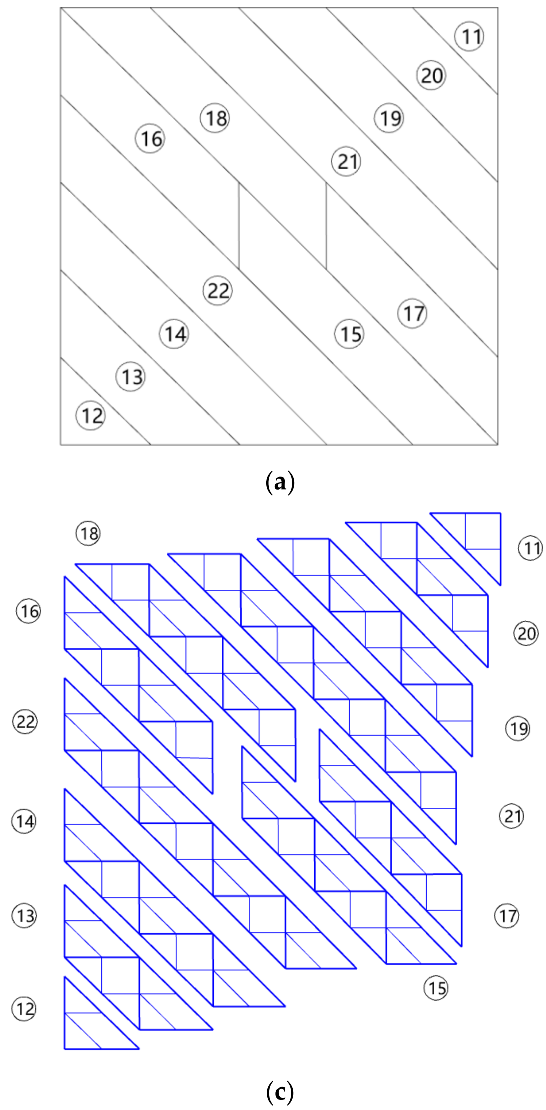

Figure 1. Numbering and decomposition diagram of the upper and lower panel. (**a**) Numbering diagram of the upper panel; (**b**) Numbering diagram of the lower panel; (**c**) Decomposition diagram of the upper panel; (**d**) Decomposition diagram of the lower panel.

The individual aluminum alloy panels alone are difficult to form stiffness perpendicular to the surface. Therefore, aluminum alloy stiffeners are installed on the underside of the lower layer aluminum alloy panel with a width of 150 mm. The stiffener strips are positioned on both sides and ends of the lower layer strip which can be directly bent from the excess allowance of the lower layer strip. The adjacent rib strips on both sides are connected together using rivets with gasket plates, making the manufacturing and installation process convenient. In the specimen, the lower layer panel consists of rectangular strips with a lack of intermediate restraint to the transverse stiffeners. To prevent local instability, stainless steel rods are placed in the middle of each elongated strip and connected to the stiffeners using bolts. The principle behind the placement of stainless steel rods is to fill in the gaps where the stiffeners are missed. Thus, when viewed from the underside, the stiffeners and stainless steel rods are combined to form a grid in the longitudinal and transverse directions, as shown in Figure 2.

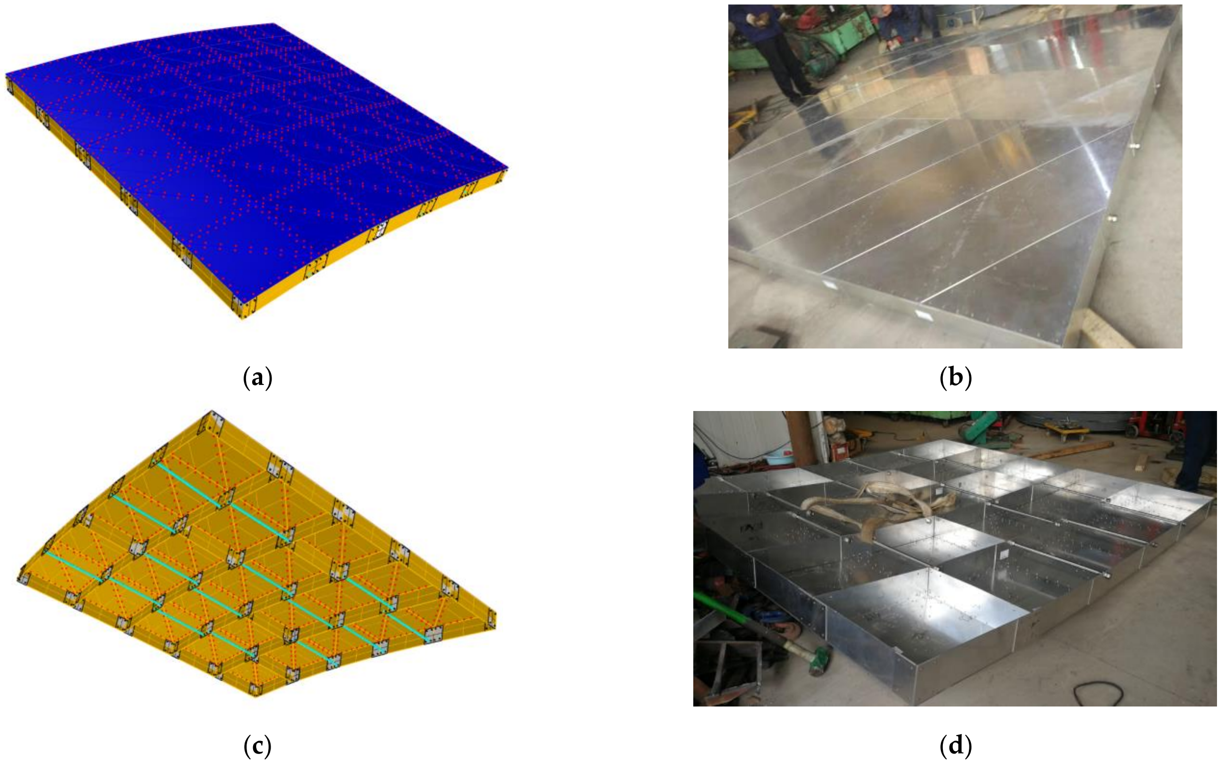

Figure 2. Axonometric view of the specimen. (**a**) Axonometric view above numerical specimen; (**b**) Axonometric view above real specimen; (**c**) Axonometric view below numerical specimen; (**d**) Axonometric view below real specimen.

The shape of the specimen resembles a unidirectional bent geometric surface where the surface structure lines in one direction are close to straight lines while the surface structure lines in the other direction form curved lines. In addition to bending in one direction, the surface also exhibits slight twisting, causing the shape of the surface structure lines to vary throughout the bending direction. This results in an irregular freeform surface.

2.2. Material Properties

In the experiment, the aluminum alloy components used 3004 alloys with a structural grade in H36 condition and a thickness of 3 mm. The specified non-proportional elongation stress is ≥190 MPa and the tensile strength is in the range of 240–285 MPa.

The rivets used for connecting the upper and lower aluminum alloy panels are Type II or Type III single-sided countersunk rivets. The rivet diameter is 4.8 mm and the hole diameter is 4.9 mm. The execution standard is Q/CRRC J24-2018.

The nuts used for connecting the stiffeners to each other as well as the stainless steel rods used to prevent instability are made of austenitic stainless steel. The material designation is S30408 and the grade is 06Cr19Ni10.

2.3. Load Reaction Frame Design

The experiment was conducted on a reaction frame which has a height of approximately 1.2 m and dimensions of 3 m × 3 m, matching the size of the specimen. The specimen was placed flat on the reaction frame. The upper part of the reaction frame had support plates that conformed to the boundary curve of the specimen and the straight boundaries were welded to the brackets according to the bending angle of the specimen's edges. The curved boundaries were determined by the supporting stiffeners spaced at intervals of 300 mm. Due to the asymmetry and non-uniform curvature of the specimen's edges, the lengths of the individual stiffeners needed to be designed based on the specific configuration of the specimen's edges. The axonometric view, side view of the reaction frame design, and profiles of the curved boundaries on both sides are shown in Figures 3 and 4.

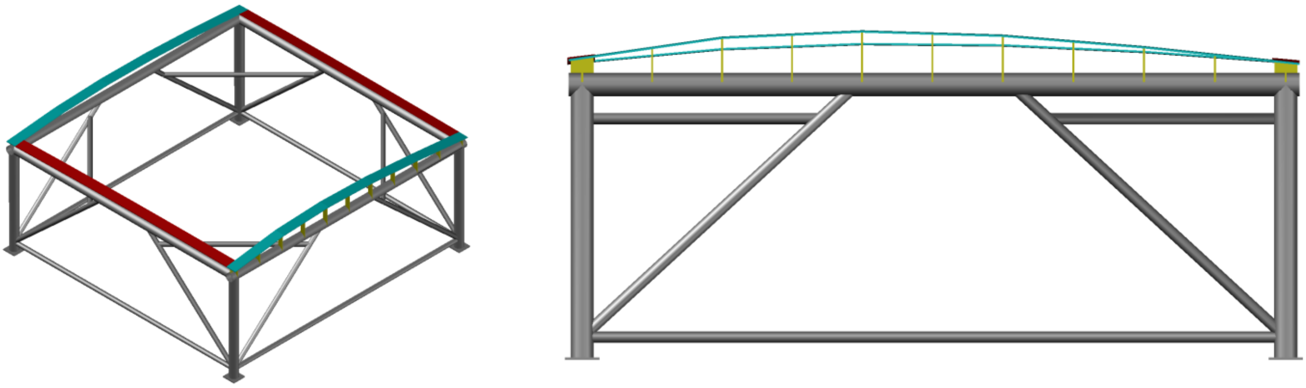

(**a**) (**b**)

Figure 3. Design of the reaction frame. (**a**) The axonometric view; (**b**) The side view.

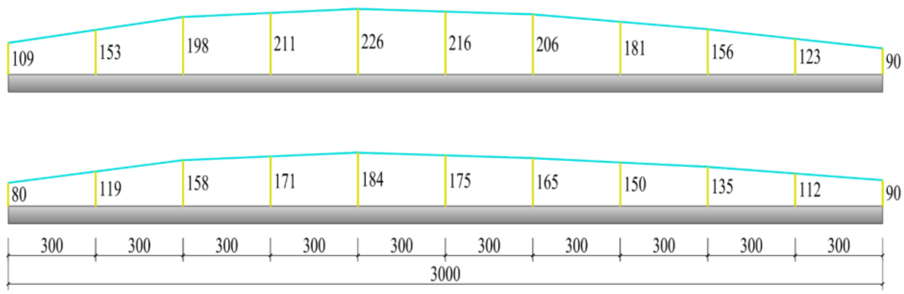

Figure 4. Profiles of the curved boundaries on both sides (mm).

The contact between the reaction frame and the specimen is achieved through direct placement, allowing the specimen to slide horizontally. To prevent excessive sliding, small rib plates are welded along two adjacent edges at right angles to restrict the horizontal displacement of the lower edge of the specimen's stiffener plates. This allows sliding on one side of the specimen while rotation the overall boundary is not restricted. The reaction frame with the installed support plates and limiting rib plates, as fabricated on-site, is shown in Figure 5.

(**a**) (**b**)

Figure 5. Partial construction of the reaction frame. (**a**) Plate of the reaction frame; (**b**) Limiting rib plates.

According to the aforementioned design of the reaction frame, the boundary conditions of the specimen are depicted in Figure 6. Two adjacent edges at right angles constrain both vertical and horizontal displacements while the other two adjacent edges only constrain vertical displacement.

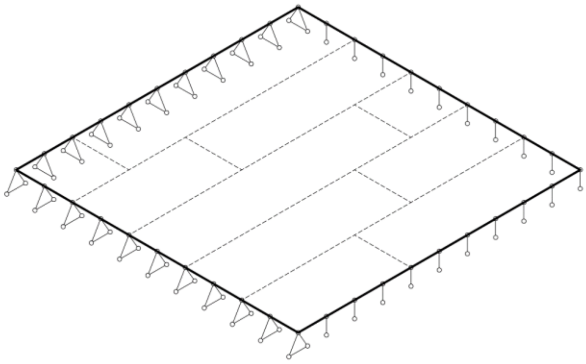

Figure 6. Boundary conditions of the specimen.

2.4. Loading Scheme

The sand stacking method was employed to achieve the maximum vertical uniformly distributed load that the panel can withstand. The main design live load considered was the snow load which was taken as 0.65 kN/m^2 based on the common snow pressure value for a 50-year return period in the northeastern provinces of China. Multiplying by the load factor of 1.5 for live load, the design value was 0.975 kN/m^2. Prior to the experiment, finite element numerical simulations were conducted and the results showed that the maximum bearing capacity of the double-layer roof panel was approximately 1.9 kN/m^2. In order to reach the failure point during the test, the load was arranged to be 2 kN/m^2, requiring a total of 1.8 tons of sand. The loading process was divided into 10 levels, with each level containing 180 kg of sand, resulting in an approximately 0.2 kN/m^2 uniformly distributed load for each level. There were 50 sandbags placed on each level, with each sandbag weighing 3.6 kg. Based on the 25 grids on the upper surface, 2 sandbags were placed in each grid for each loading level. After the completion of each loading level, a waiting period of 5 min was observed to allow for the stabilization of structural displacement before proceeding to the next level of loading, the loading process of sandbag is shown as Figure 7.

Figure 7. Stacking of the sandbag.

In order to ensure the uniformity of sand stacking, during the actual loading process, a worker weighing approximately 65 kg was on the panel to distribute and lay out the sandbag. This additional load from the worker was included in the mass considered for each level of loading. The load levels, taking into account the weight of the worker, are shown in Figure 8.

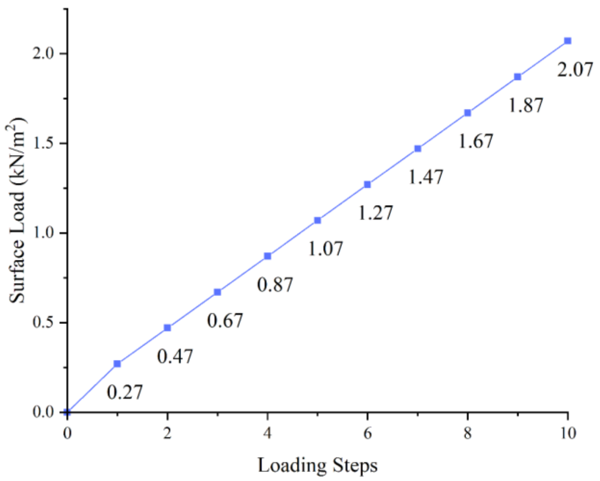

Figure 8. Loading level diagram.

2.5. Measurement Point Arrangement

During the experiment, measurements were taken for the displacement and strain of the specimen. The placement of measurement points was divided into two parts: the installation of displacement meters and the arrangement of strain gauges.

2.5.1. Displacement Meter Arrangement

The placement of displacement meters is aimed at vertical displacement measurement and horizontal displacement measurement. The vertical displacement measurement is primarily arranged within the central 3 × 3 grid area while the horizontal displacement measurement is located at the midpoint of each grid on the side edges. The diagram illustrating the placement of displacement meters is shown in Figure 9.

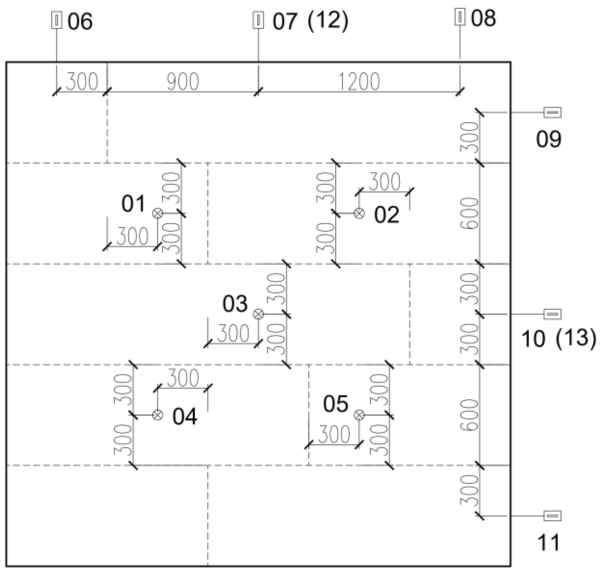

Figure 9. Placement of the displacement meters.

The displacement meters 01–05 measure the vertical displacement at the center of each grid. The displacement meters 06–13 measure the horizontal displacement outward from the edges of the specimen. Specifically, meters 06–11 are positioned near the lower edge of the stiffeners while meters 12–13 are placed near the upper edge of the stiffeners. Meters 12 and 13 serve as control points in comparison with meters 07 and 10 directly beneath them, aiming to observe any possible twisting of the edge stiffeners. All the displacement meter measurement points are located at the center of the grid or at the midpoint of the grid edges, as Figure 10 shows.

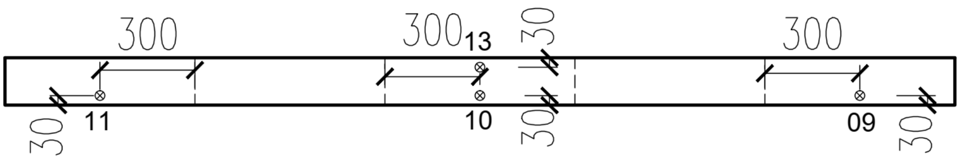

Figure 10. Arrange of edge stiffener displacement meters (right side as an example).

The five displacement meters in the middle are fixed below the specimen and they measure the displacement by pulling the line upwards. Since the horizontal displacement is restricted to zero by two side boundaries, only the displacement outward from the other two sides is measured, with 4 on each side. There are a total of 13 displacement meters, as shown in Figure 11.

(**a**)

(**b**)

Figure 11. Fixing of the displacement meter. (**a**) Vertical direction; (**b**) Horizontal direction.

2.5.2. Strain Gauge Arrangement

The strain gauges are placed on both the upper and lower surfaces of the aluminum plates using a three-axis 45° rosette configuration to measure the principal stresses and their directions within the plane at various locations.

The arrangement of strain gauges on the upper plate is shown in Figure 12. Among them, strain gauges 01–02 measure strains near the longitudinal seams, strain gauges 03–04 measure strains near the diagonal seams, and strain gauges 05–08 measure strains at the center of the diagonal plate. The strain gauges measuring strains near the seams are positioned 100 mm away from the seams while the strain gauges measuring strains at the center are located at the midpoint of the entire diagonal plate.

The arrangement of strain gauges on the lower plate is shown in Figure 13. Among them, strain gauges 01–05 measure strains at the center of each grid while strain gauges 06–07 measure strains near the longitudinal and transverse seam locations, respectively. The strain gauges measuring strains near the seams are positioned 100 mm away from the joints while the strain gauges measuring strains at the center are located at the center of the square grid.

In conclusion, a total of 15 three-axis strain gauge rosettes were installed.

Before the formal loading, the surface of the aluminum alloy plate was polished, strain gauges were attached at specified locations, displacement meters were installed, wires were connected, and the instruments were calibrated, as shown in Figure 14.

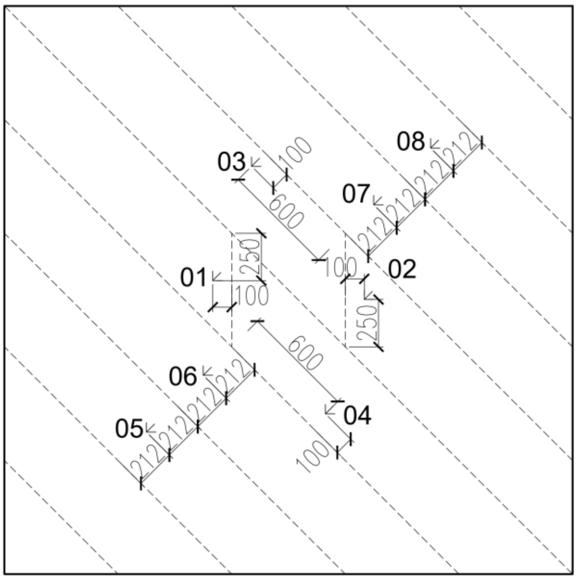

Figure 12. Arrangement of upper plate strain gauges.

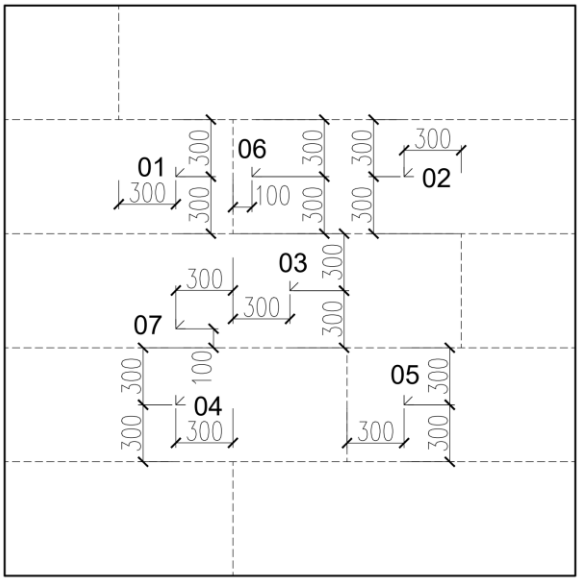

Figure 13. Arrangement of lower plate strain gauges.

Figure 14. Strain gauges paste.

3. Experiment Results

3.1. Displacement Meter Data

Tables 1 and 2 present the readings of vertical displacement meters and horizontal displacement meters at the end of each load level.

Table 1. Variation of vertical displacement with loading level.

Level	Mass (kg)	Surface Loading (kN/m^2)	1# (mm)	2# (mm)	3# (mm)	4# (mm)	5# (mm)
1	245	0.27	2	2	2	2	2
2	425	0.47	3	5	4	4	4
3	605	0.67	5	6	6	5	7
4	785	0.87	7	8	9	7	9
5	965	1.07	9	9	12	9	11
6	1145	1.27	12	11	14	11	13
7	1325	1.47	15	14	18	13	14
8	1505	1.67	19	18	22	15	16
9	1685	1.87	27	26	32	19	20
10	1865	2.07	41	36	49	26	27

Table 2. Variation of horizontal displacement with loading level.

Level	Surface Loading (kN/m^2)	6# (mm)	7# (mm)	8# (mm)	9# (mm)	10# (mm)	11# (mm)	12# (mm)	13# (mm)
1	0.27	0	0	0	0	0	0	0	0
2	0.47	0	−1	0	−1	−1	−1	−1	−1
3	0.67	0	−1	0	−1	−1	−1	−1	−1
4	0.87	0	−1	0	−1	−1	−1	−1	−1
5	1.07	0	−2	−1	−2	−2	−2	−2	−2
6	1.27	0	−2	1	−2	−3	−2	−3	−2
7	1.47	0	−2	−1	−2	−4	−2	−4	−2
8	1.67	0	−3	−1	−2	−5	−3	−5	−3
9	1.87	0	−3	−1	−3	−7	−3	−6	−4
10	2.07	0	−4	−1	−3	−9	−4	−7	−5

From Table 1, it can be observed that the maximum vertical displacement occurs at the mid-span (corresponding to displacement meter 3#), reaching 49 mm when the external load is 2.07 kN/m^2. The maximum horizontal displacement of the entire roof panel occurs above the right-side stiffener (corresponding to displacement meter 10#) with an out-of-plane deformation of 9 mm when the external load is 2.07 kN/m^2.

3.2. Specimen Displacement Mode

Displacement meters 1–5 measured the downward displacement at the center of the specimen. The arrangement diagram and the displacement–loading curve are shown in Figure 15.

From Figure 15, it can be observed that due to the uneven distribution of the stiffeners, the displacement values vary at different locations. Among them, the displacement at the center is the largest, corresponding to displacement meter 3. Among the four displacement meters around the center, meters 1 and 2 show relatively larger displacements compared to the other side. The displacement pattern at the center of the specimen is similar to that of a simply supported rectangular plate.

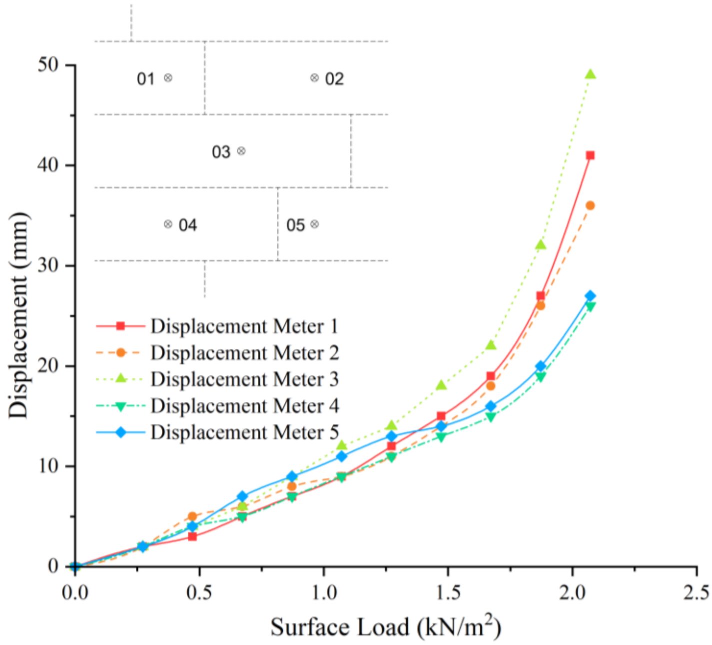

Figure 15. Displacement–loading curves of displacement meters 1–5.

Displacement meters 6–13 measured the outward displacement at the sides of the specimen. Taking the right side as an example, the arrangement diagram and the displacement–load curve are shown in Figure 16.

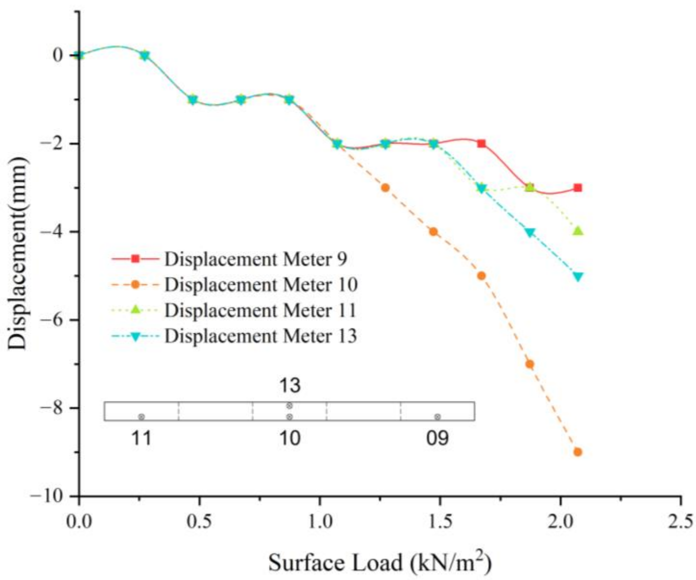

Figure 16. Displacement–loading curves of displacement meters on the right side.

From Figure 16, it can be observed that there is not much difference in displacements between meters 9, 11, and 13. However, displacement meter 10 in the middle of the lower section shows a significantly larger displacement compared to the other three meters, indicating a significant twisting deformation occurring in the middle of the lateral stiffener.

Images capturing the post-loading displacement patterns at the center and sides of the specimen were also taken on-site, as shown in Figure 17.

(**a**)

(**b**)

Figure 17. Middle and lateral displacement of the specimen. (**a**) Middle displacement of the specimen; (**b**) Lateral displacement of the specimen.

Based on the above results, the displacement patterns and force transmission modes during the loading process of the specimen can be determined, as shown in Figure 18.

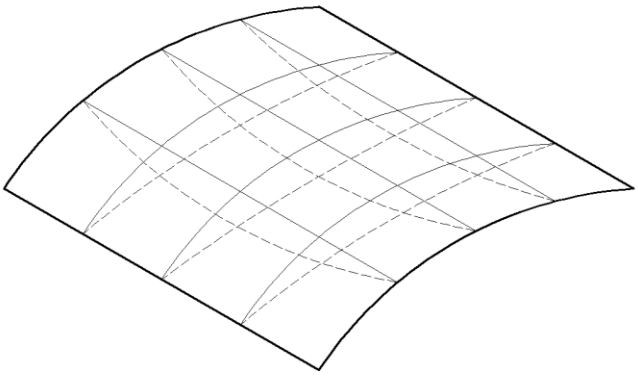

(**a**)

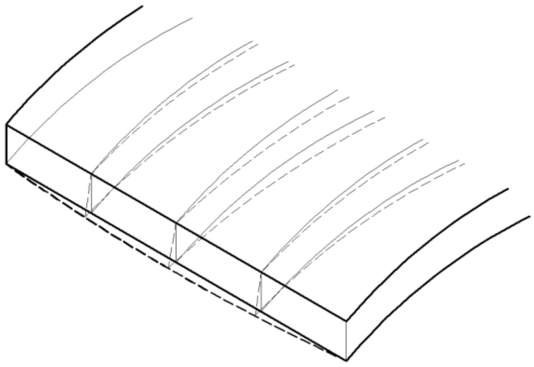

(**b**)

Figure 18. Central and lateral displacement pattern of the specimen. (**a**) Central displacement pattern of the specimen; (**b**) Lateral displacement pattern of the specimen.

Under the action of the load, the central part of the specimen experiences downward displacement with larger displacements in the middle and smaller displacements on the periphery. The upper and lower aluminum plates in the central part of the specimen undergo bending together with the upper plate experiencing compression and the lower plate experiencing tension under the load. Due to the length-throughout stiffeners in transverse direction, the displacement of the lower plate is transferred to these stiffeners in transverse direction, resulting in bending of the stiffeners in a transverse direction. As a result, significant downward displacement occurs in the middle of these stiffeners. Subsequently, this leads to larger outward displacements in the lower part of the outer-side stiffeners at the side positions, indicating torsion of the outer-side stiffeners.

3.3. Strain Gauge Data

In the experiment, three-axis 45° strain gauge rosettes were used to measure the strain of the upper and lower layers of the roof panels. Based on the measurement principle of this type of strain gauge rosette, assuming the strains measured by the three strain gauges are ε_0, ε_{45}, and ε_{90}, as shown in Figure 19, the principal strain and principal stress at that location can be calculated by Equations (1) and (2). Additionally, the angle α between the principal stress and the horizontal line at 0° can be calculated using Equation (3).

$$\begin{matrix}\varepsilon_1 \\ \varepsilon_2\end{matrix} = \frac{\varepsilon_0+\varepsilon_{90}}{2} \pm \frac{\sqrt{2}}{2}\sqrt{(\varepsilon_0-\varepsilon_{45})^2+(\varepsilon_{45}-\varepsilon_{90})^2} \quad (1)$$

$$\begin{matrix}\sigma_1 \\ \sigma_2\end{matrix} = \frac{E}{2}\left[\frac{\varepsilon_0+\varepsilon_{90}}{1-\nu} \pm \frac{\sqrt{2}}{1+\nu}\sqrt{(\varepsilon_0-\varepsilon_{45})^2+(\varepsilon_{45}-\varepsilon_{90})^2}\right] \quad (2)$$

$$\alpha = \frac{1}{2}arctg\frac{2\varepsilon_{45}-\varepsilon_0-\varepsilon_{90}}{\varepsilon_0-\varepsilon_{90}} \quad (3)$$

In the equations, ε_1 and ε_2 represent the maximum and minimum principal strains, σ_1 and σ_2 represent the maximum and minimum principal stresses, E is the elastic modulus of the aluminum alloy material, taken as 70,000 MPa, and ν is the Poisson's ratio, taken as 0.3.

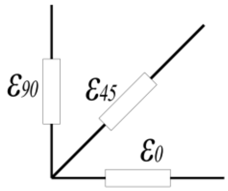

Figure 19. Three-axis 45° strain gauge rosette.

Tables 3 and 4 present the results of the principal stresses at the strain gauge positions calculated based on the readings from the strain gauges (the principal stress is taken as the one which has a larger absolute value).

Table 3. Variation of the principal stress on the upper surface (σ_2) with loading level.

Level	Surface Loading (kN/m^2)	1# (mm)	2# (mm)	3# (mm)	4# (mm)	5# (mm)	6# (mm)	7# (mm)	8# (mm)
1	0.27	−2.29	−3.23	−1.79	−1.73	−2.69	−3.94	−3.92	−2.91
2	0.47	−2.75	−4.69	−2.39	−3.80	−4.94	−7.37	−5.71	−4.12
3	0.67	−2.28	−6.13	−3.44	−6.09	−6.06	−8.04	−6.74	−4.33
4	0.87	−2.98	−8.41	−3.99	−6.59	−7.17	−11.15	−11.02	−7.47
5	1.07	−3.08	−10.19	−4.60	−6.38	−7.91	−12.79	−11.19	−7.32
6	1.27	−3.14	−8.36	−5.94	−9.44	−7.78	−14.71	−13.42	−8.23
7	1.47	−3.91	−15.10	−6.61	−9.16	−9.48	−15.70	−15.47	−9.69
8	1.67	−4.77	−11.38	−7.24	−12.92	−13.21	−19.06	−17.97	−12.15
9	1.87	−23.15	−23.88	−8.48	−16.14	−16.22	−22.40	−24.24	−14.20
10	2.07	−21.17	−35.92	−9.66	−17.82	−23.23	−27.40	−30.41	−18.26

Table 4. Variation of the principal stress on the lower surface (σ_1) with loading level (7# take σ_2 principal stress).

Level	Surface Loading (kN/m^2)	1# (mm)	2# (mm)	3# (mm)	4# (mm)	5# (mm)	6# (mm)	7# (mm)
1	0.27	3.86	2.88	6.02	6.52	7.58	0.61	−1.76
2	0.47	18.92	8.75	8.84	10.77	12.86	2.04	−2.73
3	0.67	22.00	10.52	13.25	12.94	18.27	2.43	−2.43
4	0.87	28.69	13.05	16.10	21.82	23.03	3.00	−3.25
5	1.07	25.65	17.18	16.59	25.17	24.93	3.91	−3.53
6	1.27	30.61	18.05	22.47	29.90	28.79	5.08	−3.12
7	1.47	39.41	22.62	26.73	34.97	33.20	5.08	−3.28
8	1.67	48.69	25.75	30.77	38.35	34.94	9.49	−4.18
9	1.87	61.71	30.90	45.80	42.72	42.23	7.80	−6.07
10	2.07	77.58	35.38	52.94	44.66	51.18	10.98	−13.15

From Tables 3 and 4, it can be observed that there is a significant difference in the stress state between the upper and lower layers of the panels: the upper layer is mainly under compression, with the maximum principal stress being compressive stress, while the lower layer is mainly under tension, with the maximum principal stress being tensile stress. Overall, the upper and lower layers of the panels are subjected to bending together and their stress states are similar to those of a simply supported plate on the upper and lower surfaces.

In the upper layer, strain gauges 1–4 are located near the seams and strain gauges 5–8 are located at the center of the strip. In the lower layer, strain gauges 1–5 are located at the center of the grid and strain gauges 6–7 are located near the stiffeners. From the data in the two tables, it can be observed that there is no significant stress concentration near the seams or near the stiffeners. The difference in stress level between these areas and the center of the strip/grid is not significant. The maximum principal stresses at all locations are far below the yield strength of 190 MPa. Within the 10 levels of loading, there is no plastic deformation observed in any strain measurement position of the upper and lower aluminum alloy plates.

3.4. Panel Stress Analysis

By using Equations (2) and (3), the magnitude and direction of the principal stresses at each strain gauge measurement point can be calculated. By scaling the principal stresses according to their magnitudes, the stress states of the upper and lower aluminum alloy panels at each location (when the specimen is about to fail) can be plotted on a single graph, as shown in Figure 20.

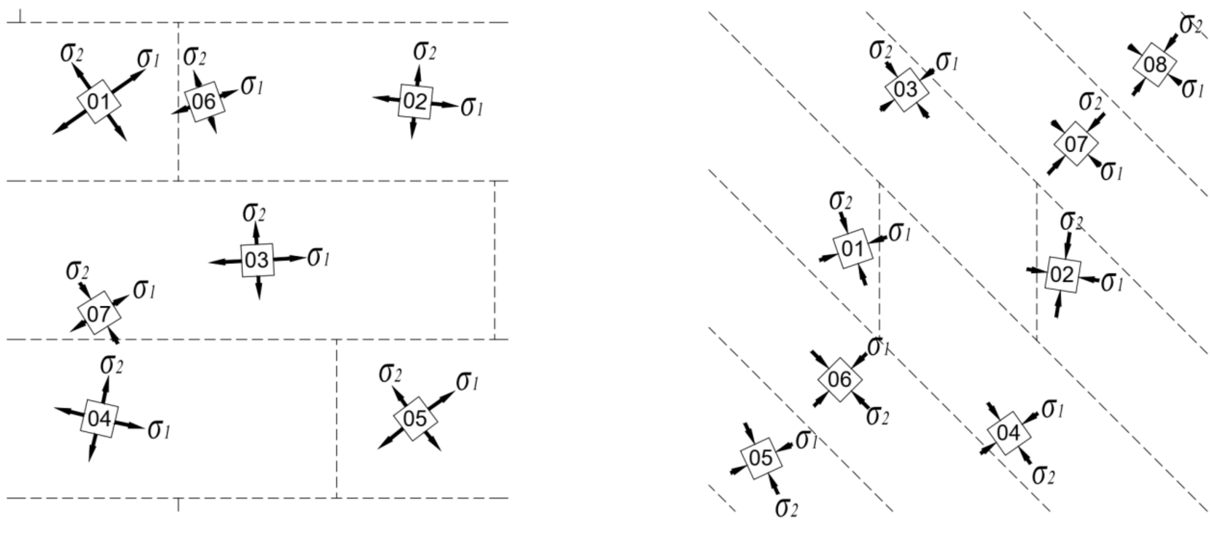

Figure 20. Stress state diagram for upper and lower panels. (**a**) Stress state diagram for upper panel; (**b**) Stress state diagram for lower panel.

From Figure 20, it can be observed that the upper panel is mainly subjected to biaxial compressive stress while the lower panel experiences biaxial tensile stress. For the upper panel, the stress near the stiffeners is relatively small, as seen in measurement points 01, 03, and 04. The stress at position 02, where the vertical displacement of the panel is maximum, is slightly larger. The stress at measurement points within each panel strip near the center of spans (05–08) is higher than that near the stiffeners, and the stress increases closer to the center of spans. The principal stress directions at the span centers are nearly parallel to the panel strips.

Similar patterns can be observed for the lower panel. The stress is smaller at measurement points 06 and 07 near the stiffeners while it is higher at other central locations within the grid. The principal stress direction also varies with the measurement point's location. Measurement points 01 and 05 resemble three-side-supported panels with principal stress directions closer to a 45° diagonal. Measurement points 02, 03, and 04 resemble two-side-supported panels with principal stress directions closer to the 0° direction. Additionally, in the direction of the panel strip's extension, the principal stress is higher.

Based on the qualitative analysis above, it can be inferred that the stress state of the panels is influenced by factors such as the stiffeners, the dimensions of the panel strips, and the support conditions. Moreover, at positions where the out-of-plane displacement is larger, the stress is also higher. The stiffeners not only resist tension in conjunction with the lower panel, reducing the stress level near them, but also provide support and separation for the double-layer panels, influencing the in-plane principal stress directions.

3.5. Specimen Failure Mechanism

During the actual loading process, after completing the first 10 loading levels, the upper part of the specimen was subjected to a load of 2.07 kN/m^2. At this point, the specimen had not yet failed. Subsequently, additional loading was applied, totaling 423 kg, which is equivalent to a distributed final load of 2.54 kN/m^2 (although the actual load effect is greater than this distributed value since the subsequent loading was mainly concentrated on the central part of the specimen and not uniformly distributed). Under this load level, the lower part of the central section of the specimen approached failure, with the stiffeners in a shearing damage state by rivets. A photograph of the site is shown in Figure 21.

(**a**) (**b**)

Figure 21. Damage to the specimen at the stiffener location. (**a**) Side view of the damaged location; (**b**) Bottom view of the damaged location.

This failure mode is consistent with the displacement pattern analyzed in Section 3.2. The lower part of the central section of the specimen experiences predominantly bending moments which are primarily borne by the lower portion of the stiffeners. Under the action of these bending moments, the stiffeners gradually transition from an upward bending shape to a horizontal and then a downward bending shape. During this process, the lower part of the stiffeners undergoes significant displacement. When this location is pulled wide enough, the aluminum plate of the stiffeners is sheared by the rivets as the strength of the rivets is greater than that of the stiffeners' aluminum plate.

4. Finite Element Numerical Simulation

4.1. Material Properties and Element Selection

Numerical simulations on the static loading of aluminum roof panels were carried out in ABAQUS 6.14 software (produced by Dassault Systemes, Paris, French), a general-purpose finite element software. The upper and lower aluminum alloy panels have a thickness of 3 mm each and their material grade is 3004-H36. Shell elements are used for simulation and the panel is divided into nine integration points along the thickness with a spacing of 3 mm to ensure tight contact between the two panels. The material strength of the panels is determined according to the " Aluminum Alloy Structural Design Specification" (GB 50429-2007), with an elastic modulus of E = 70,000 MPa and a Poisson's ratio of v = 0.3. The stainless steel rod is of austenitic type, S30408, and its elastic modulus is taken as E = 193,000 MPa based on the regulations of "Technical Specification for Stainless Steel Structures" (CECS 410:2015) and it is simulated using beam elements.

4.2. Mesh Division, Boundary, Contact, and Load Settings

In the finite element model, nodes were created at the corresponding positions of the riveted connections between the two panels. It was ensured that the mesh division of the two panels was completely identical using triangular elements. The maximum edge length of the mesh was 70 mm, as shown in Figure 22. The red dots in the figure represent the corresponding positions of the riveted connections.

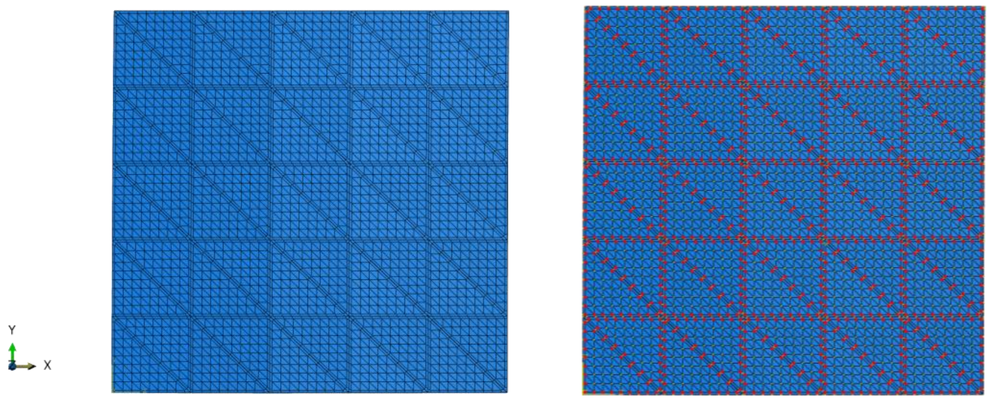

Figure 22. Finite element model aluminum plate meshing and rivet location.

The "Tie" constraint was applied at the connection nodes between the two panels. The stainless steel rod and the stiffener plate were connected using the "MPC-PIN" hinge constraint, as Figure 23 shows.

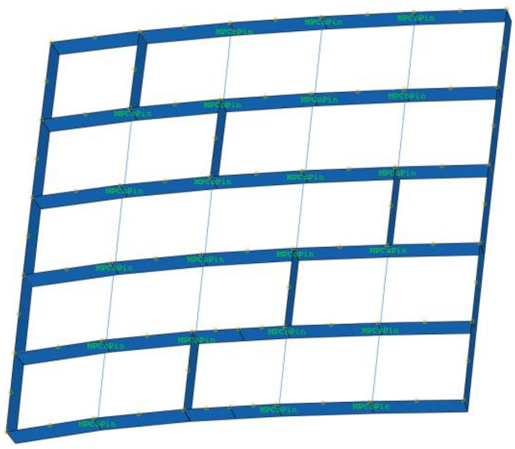

Figure 23. Connection of stainless steel rods to stiffeners.

Vertical displacements (in the Z direction) of the bottom edges of the four stiffener plates were constrained. Additionally, to prevent horizontal movement of the entire structure, horizontal constraints (in the XY direction) were applied to the corner points, as shown in Figure 24. The applied load on the panel surface is vertically downward and consists of two components: a concentrated load applied at the center of the panel corresponding to the weight of a worker and a uniformly distributed pressure load applied in 10 levels. The loading levels applied follow the loading levels during the experiment shown in Figure 8.

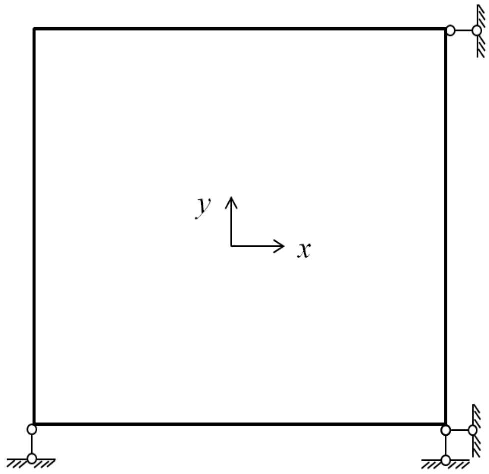

Figure 24. Horizontal boundary condition in the finite element model.

4.3. Analysis of Simulation Results

Two finite element models were established, one with a single-layer panel and the other with a double-layer panel riveted together. The single-layer panel model employed the same stiffener arrangement as the double-layer panel experiment. The results of both models were compared to validate the effect of using a double-layer construction on the load-bearing capacity.

Figure 25 shows the von Mises stress contour plots for the single-layer model's panel and the upper and lower panels of the double-layer model under ultimate load-carrying capacity. From the perspective of ultimate load-carrying capacity, the maximum uniform distributed pressure that the single-layer panel model can withstand is 1.2 kN/m^2. The stress distribution on the panel is uneven, with most of the panel stresses below 50 MPa, but localized stress peaks of approximately 150 MPa appear in the areas connected to the stiffeners. The double-layer panel can withstand a maximum uniform distributed pressure of 1.9 kN/m^2. The overall stress level on the upper and lower panels is relatively low, with most of the panel stresses below 50 MPa. However, there is some stress concentration at the locations of the local stiffeners or diagonal seams. The maximum stress in the double-layer panel model occurs at the midpoint of the transverse stiffener where there is a lack of longitudinal stiffener constraint, reaching 215 MPa. This failure mode is consistent with the experimental results.

Figure 26 shows the vertical displacement contour plots corresponding to the ultimate load-carrying capacity. The displacement patterns of the single-layer panel and the double-layer panel are very similar, with the maximum displacements located in the two least vertical stiffness grid squares in the middle and right side. The maximum deflection of the single-layer panel model is 42 mm while the maximum deflection of the double-layer panel model is 31 mm. This indicates that the displacement pattern of the panel is mainly influenced by the arrangement of stiffeners and the vertical stiffness of the panel is not only affected by the stiffeners but also closely related to the composition of the panel. The construction of the double-layer panel significantly improves its vertical stiffness.

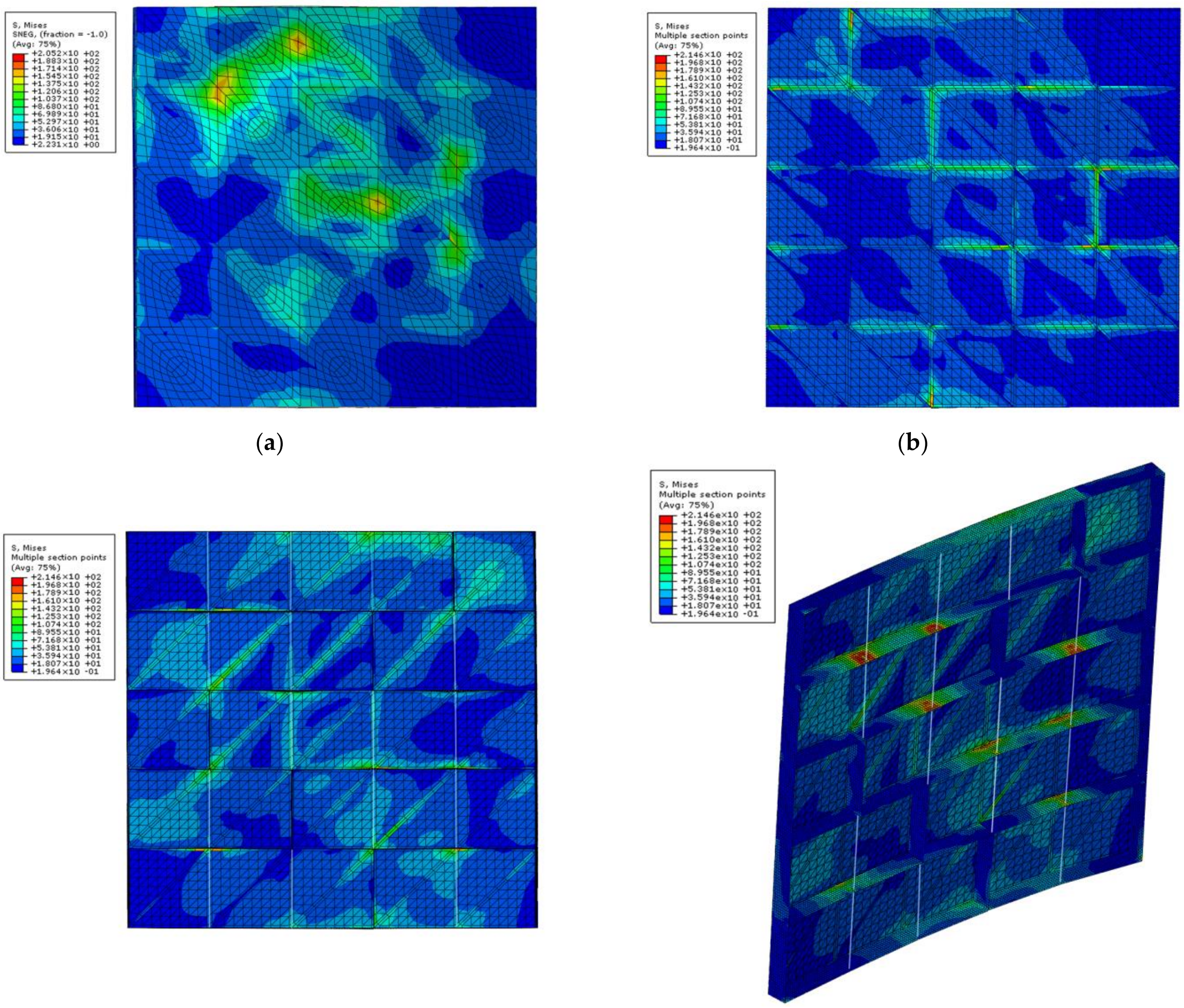

(**a**) (**b**) (**c**) (**d**)

Figure 25. Mises stress contour plots at ultimate load-carrying capacity. (**a**) Single-layer Mises stress; (**b**) Double-riveted-layer upper plate Mises stress; (**c**) Double-riveted-layer lower plate Mises stress; (**d**) Double-riveted-layer stiffener Mises stress.

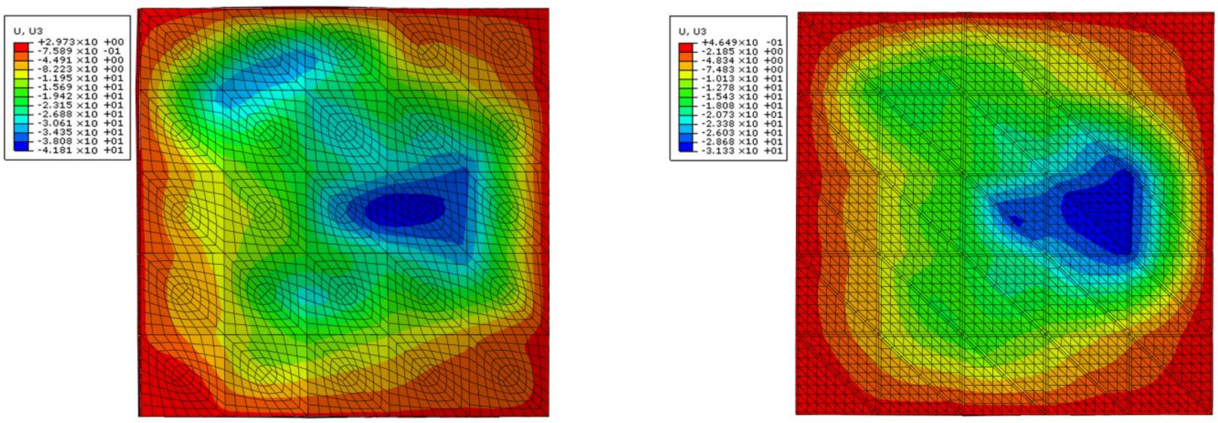

(**a**) (**b**)

Figure 26. Vertical displacement contour plots at ultimate load-carrying capacity. (**a**) Vertical displacement of single-layer; (**b**) Vertical displacement of double-riveted-layer.

Figure 27 shows the U1 displacement contour plots in the horizontal plane corresponding to the ultimate load-carrying capacity. In the single-layer panel model, the maximum displacement occurs at the outer edge on one side and at the location with the maximum displacement at the mid-span. In the double-layer panel model, the maximum displacements occur at the outer edges on both sides. This displacement distribution is related to the overall displacement pattern of the model: the transverse stiffeners experience bending behavior due to the forces transmitted from the panel and when reaching the outer edges it results in torsion of the outer edge stiffeners which is consistent with the experimental results. In the single-layer panel model, due to the large displacement at the mid-span and the separation constraint provided by the longitudinal stiffener on one side, the maximum negative displacement occurs near the mid-span rather than at the outer edge.

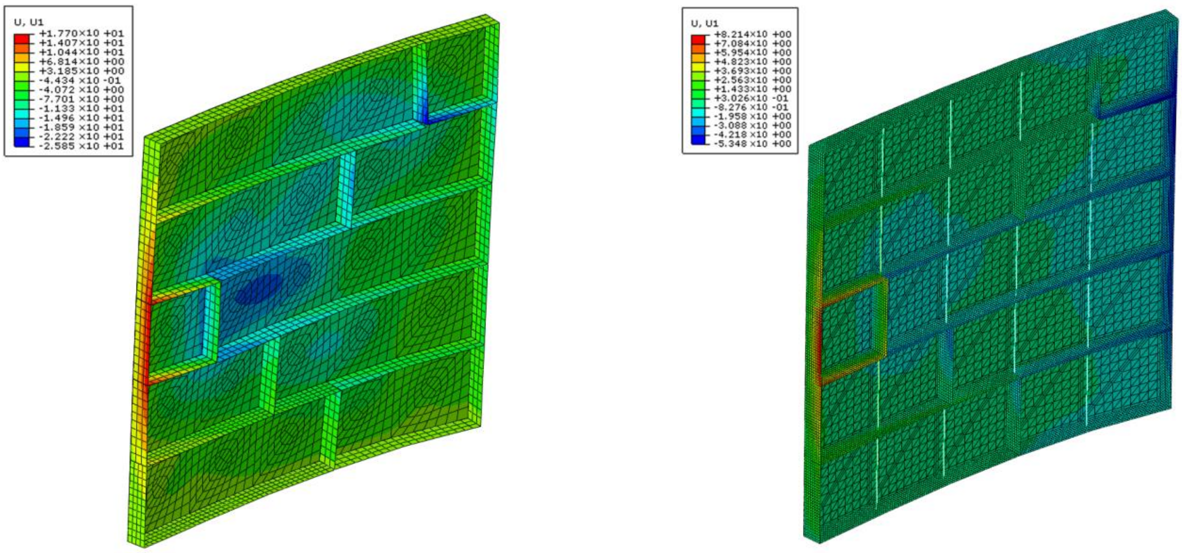

(**a**) (**b**)

Figure 27. U1 displacement contour plots at ultimate load-carrying capacity. (**a**) U1 displacement of single-layer; (**b**) U1 displacement of double-riveted-layer.

Figure 28 shows the U2 displacement contour plots in the horizontal plane corresponding to the ultimate load-carrying capacity. The maximum displacements in both the single-layer and double-layer panel models occur at the outer edge positions and twisting phenomena are observed in the outer edge stiffeners. When comparing the single-layer and double-layer panel models, in both the U1 and U2 directions, the displacements of the double-layer panel are smaller than those of the single-layer panel. This is because the double-layer panel and stainless steel bars enhance the overall bending stiffness of the model, reducing the bending deformation of the stiffeners. When comparing the U1 and U2 displacements, the U1 displacement of the single-layer panel is slightly greater than the U2 displacement. This is because the transverse stiffeners associated with U1 span the entire length of the model, serving as the main bending components and experiencing larger bending moments and resulting in greater bending deformation. On the other hand, the longitudinal stiffeners associated with U2 are sparsely distributed along the span, providing constraints to the transverse stiffeners and bearing less bending moment and resulting in smaller bending deformation at the side edges. In the case of the double-layer panel, the difference between the U1 and U2 displacements is much smaller because the stainless steel bars, in combination with the longitudinal stiffeners, provide bending stiffness in the U2 direction. From the above analysis, it can be concluded that the inclusion of stainless steel bars not only provides constraints to the transverse stiffeners, preventing local buckling, but also ensures more uniform stiffness in both directions of the panel, optimizing the bending resistance behavior of the model.

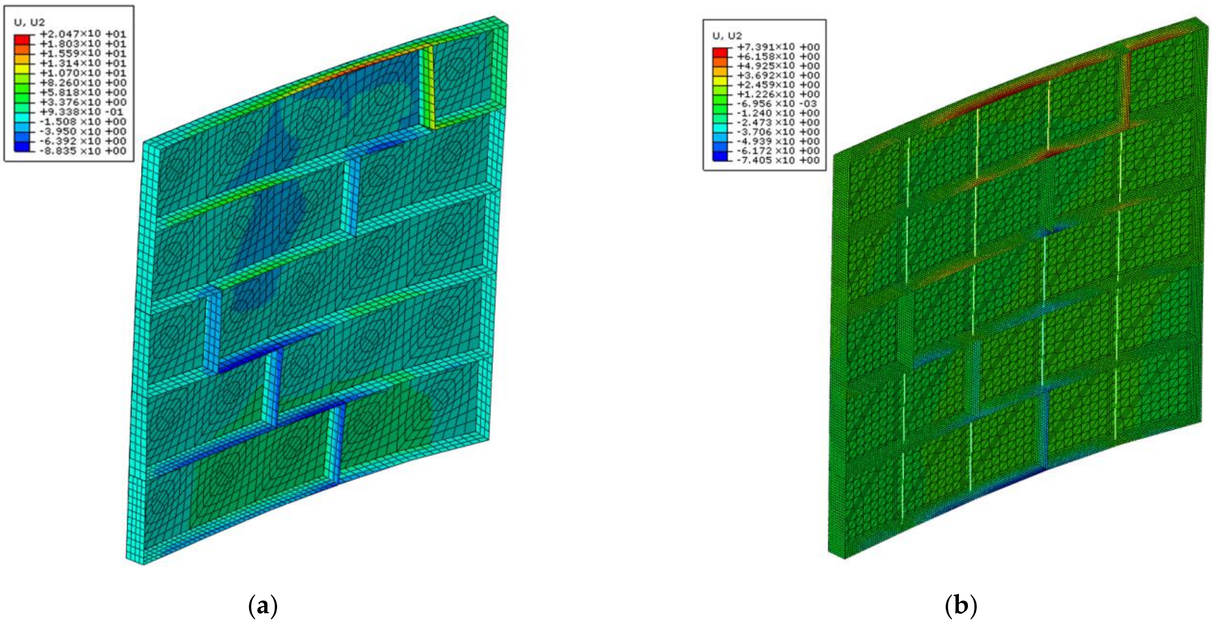

Figure 28. U2 displacement contour plots at ultimate load-carrying capacity. (**a**) U2 displacement of single-layer; (**b**) U2 displacement of double-riveted-layer.

Displacement data from displacement meter 3 at the center position of the specimen were selected to plot the load–displacement curves along with the load–displacement curve obtained from the finite element model calculations, as shown in Figure 29. A comparison between the two reveals a good agreement within the loading range of 10 levels, indicating a close correlation between the finite element results and the experimental results. However, the ultimate load obtained from the experiment exceeds the simulated value obtained from the finite element analysis.

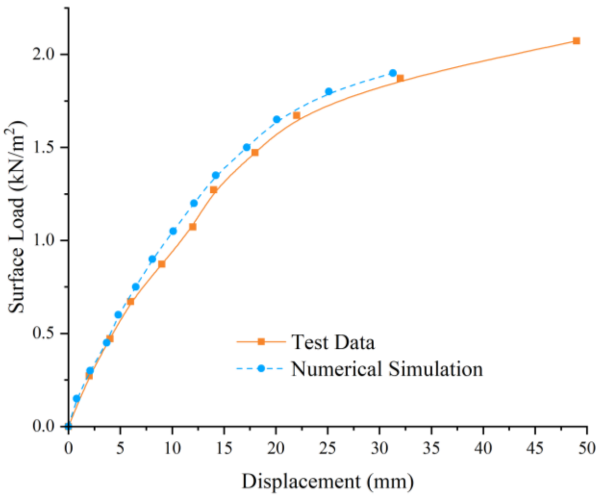

Figure 29. Comparison of finite element and experiment load–displacement curves.

5. Theoretical Analysis of Load-Bearing Capacity

5.1. Plate Zone Division and Boundary Conditions

The lower layer of the roof panel is constructed by dividing the panel and bending it to form stiffeners, as shown in Figure 30a. Since only one stiffener is set in each vertical plane, there are two types of connections: one where the panel edge is connected to the bent stiffener and another where the panel edge is disconnected from the stiffener. In the case of disconnected connections, the continuity of the panel is ensured by riveting between the upper layer and the lower layer panel. In terms of specific construction, each stiffener is connected to the lower layer on one side and disconnected from the lower layer on the other side, as shown in Figure 30b. The connected side allows the upper and lower layers to jointly withstand the bending moment of the panel edge so it can be approximated as a fixed support. The disconnected side only allows the upper layer to bear and transmit the tensile and shear forces of the panel so it can be approximated as a hinged support.

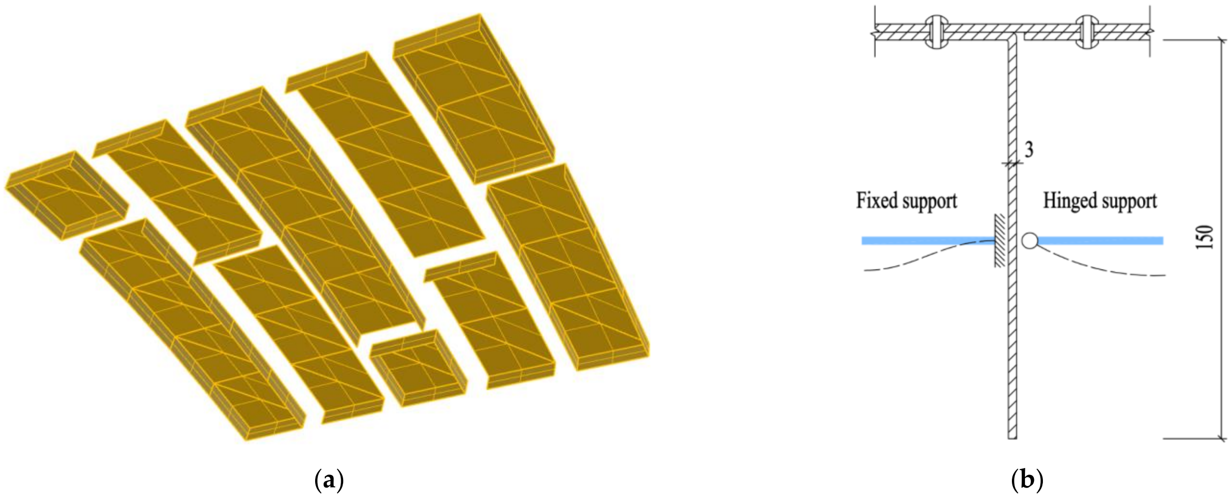

Figure 30. Separation and construction of the lower panel. (**a**) Lower panel compartment; (**b**) Two types of construction.

Based on the assumptions above, the square grid of the roof panel can be divided into up to seven types based on different boundary conditions. These seven types represent all the possibilities for grid division in this type of roof panel design, as shown in Figure 31. In the diagram, the boundaries represented by diagonal lines at 45° represent fixed supports, dashed lines parallel to the boundaries represent hinged supports, and blank boundaries represent no supports. Referring to Figure 30, the positions of these seven types of grid divisions on the panel surface can also be identified.

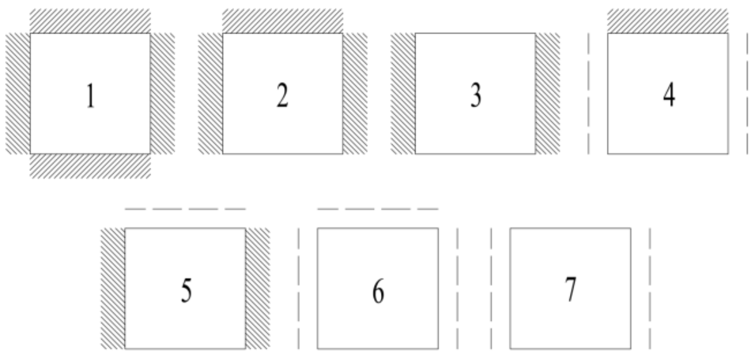

Figure 31. Panel square boundary type.

The seven types of grid divisions include the following. 1. Four sides fixed support; 2. Three sides fixed support; 3. Opposite sides fixed support; 4. One side fixed support and two sides hinged support; 5. One side-hinged support and two sides fixed support; 6. Three sides hinged support; 7. Opposite sides hinged support.

5.2. Plate Surface Load Distribution

Different boundary types result in different load distribution and conduction paths. Generally, fixed support boundaries provide more constraints compared to hinged support boundaries, resulting in a higher load distribution from the plate surface. When calculating the load distribution on the plate surface, two commonly used methods are precise analytical methods and geometric simplification methods. Analytical methods provide accurate plate edge load distributions but are complex and involve multiple parameters. Simplification methods are often used for load distribution on concrete slabs where an approximate load function is assumed and the load is distributed to beams based on area.

The main focus of this study is the distribution of vertical loads on the plate surface. For ease of calculation, a simplification method is employed to distribute the load to the surrounding stiffeners of the grid. Referring to the calculation method used for concrete slabs, for each point on the plate surface, the nearest boundary support can be identified. Points that are equidistant from both boundaries are considered to be critical points; all critical points form a critical curve, dividing the plate surface into different load-carrying regions.

To reflect the different load-carrying effects of different boundary conditions, when a point on the plate surface has two different adjacent boundaries, one of the distances should be multiplied by an amplification factor for comparison. During load distribution, the fixed support boundary carries a larger area. Therefore, the distance from a point to the hinged support boundary needs to be multiplied by the amplification factor. In other words, the coordinates of the critical points on the plate surface satisfy the condition of Equation (4), where "a" represents the distance from the point to the nearest fixed support boundary, "b" represents the distance from the point to the nearest hinged support boundary, and "γ" represents the amplification factor. When the closest boundaries of a point have the same type, the amplification factor is not considered.

$$a = \gamma \cdot b \tag{4}$$

The amplification factor reflects the distribution pattern of load transfer to different boundaries and can be determined through numerical calculations. In the ABAQUS software, by modeling the square plate with specific dimensions and corresponding load levels from the experiment with different boundary conditions (using shell elements for the plate), the vertical load values and distributions on each boundary can be obtained through calculations. Calculation and support reaction force statistics were conducted for the seven types of square plates and it was found from the analysis that the amplification factor γ can be approximated as 2.0. This yields the load distribution on the plate surface as shown in Figure 32, where "q" represents the load density on the plate surface and "l" represents the size of the square grid. It can be observed that the line loads transferred to the stiffeners mainly consist of triangular loads, trapezoidal loads, and uniformly distributed loads, with their values depending on the boundary conditions. The total vertical reaction forces on the boundaries were calculated according to the load distribution shown in Figure 32 and the results were compared with the numerical calculations. The difference was within 10% and the shape of the reaction force distribution from the numerical calculations was similar to that shown in Figure 32. This indicates that the load distribution provided by the simplified method is approximately accurate and can be used for subsequent calculations.

5.3. Calculation of Stiffener Bending Moments

The load on the plate surface is transferred as line loads to the stiffeners which serve as the primary bending components of the model and play a similar role to curved beams in bearing the load. The stiffeners consist of continuous transverse stiffeners and spaced longitudinal stiffeners. The transverse stiffeners can be seen as simply supported curved beams with five spans while the longitudinal stiffeners within each span can be considered fixed-end beams.

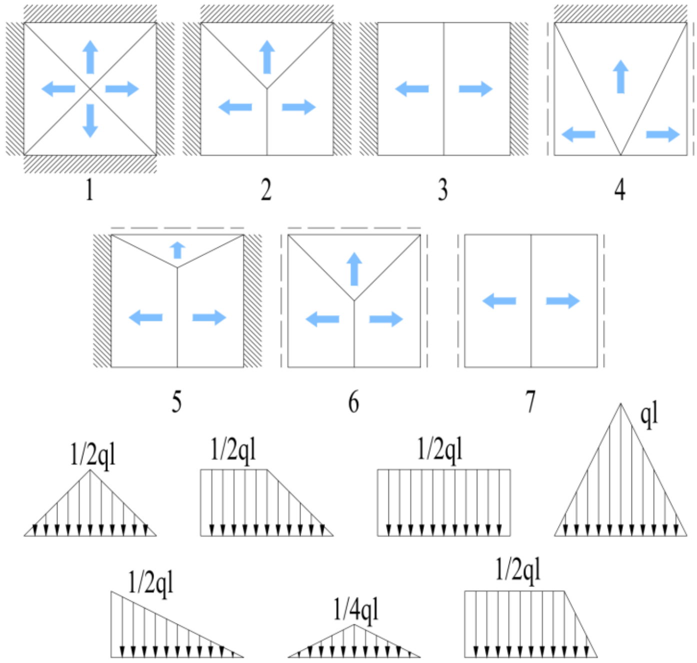

Figure 32. The panel load distribution with an amplification factor of 2.0.

Within the spans of the panel, there are spaced longitudinal stiffeners and stainless steel bars as out-of-plane constraints for the transverse stiffeners. The stainless steel bars are installed on the underside of the transverse stiffeners, allowing vertical displacements to occur easily along with the transverse stiffeners, resulting in little vertical constraint to the transverse stiffeners. The longitudinal stiffeners extend from the side of the model and are inserted sequentially into the gaps between the transverse stiffeners. Since the longitudinal stiffeners can effectively transmit shear forces, they provide some vertical constraints for the transverse stiffeners. From Figure 33, it can be observed that the arranged longitudinal stiffeners, in conjunction with the transverse stiffeners, form two diagonal line influence zones on the plate surface. Within these influence zones, the transverse stiffeners are subjected to a certain degree of vertical constraint. Therefore, for the first and second transverse stiffeners, the locations intersecting with the influence zones can be approximated as having vertical support constraints, dividing the transverse stiffeners into a 1, 4 span continuous beam. The intersection positions of the third and fourth transverse stiffeners with the influence zones are closer to the mid-span. In comparison, the support positions on the first and second stiffeners are more unfavorable for bearing moments. Therefore, the moment results for the third and fourth stiffeners are not calculated.

According to the plate load distribution theory in Section 5.2, combined with the support conditions of the plate surface on both sides of the stiffeners shown in Figure 30a, line loads distributed and transmitted to both sides of the 1 and 2 transverse stiffeners can be plotted, as shown in Figure 34. By establishing a curved beam model based on the actual geometric dimensions of the stiffeners, defining supports and considering the self-weight of the aluminum roof panels as a uniform line load, the internal forces of each section of the curved beam can be calculated. The results indicate that the maximum positive bending moment occurs near the mid-span node on the right side of transverse stiffener 1. The moment at that section is 701 N·m, the axial force is −85 N, and the shear force is −95 N.

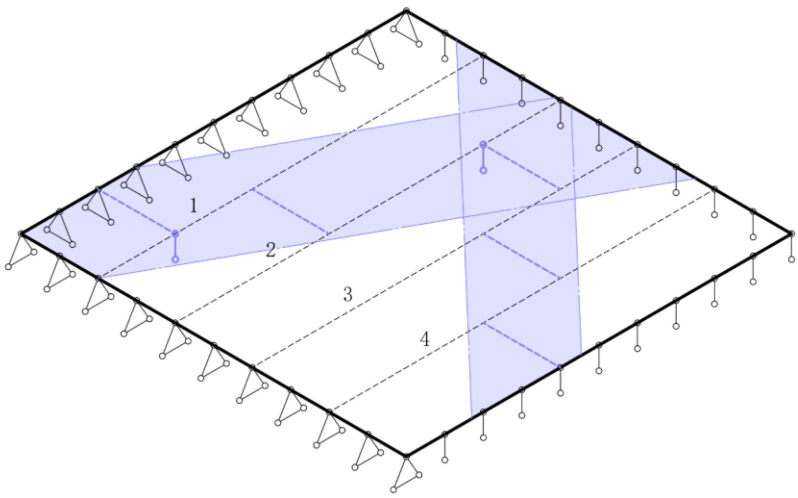

Figure 33. Restraining effect of longitudinal stiffeners on transverse stiffeners.

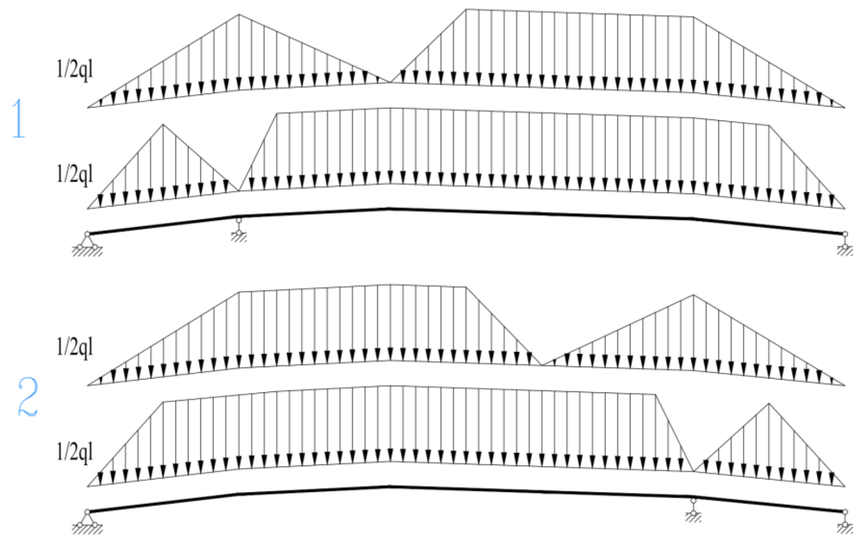

Figure 34. Line load arrangement on 1, 2 transverse stiffeners.

5.4. Rivet Shear Damage Calculation

In the previous section, the transverse stiffeners were assumed to be curved beams for calculating internal forces. Indeed, at the mid-span, it is reasonable to approximate the transverse stiffeners as bending-resistant beam sections. However, between the adjacent transverse stiffeners, i.e., at the nodes of the curved beam, they are connected using side plates and rivets, as shown in Figure 35. The bending moment on the stiffener on one side is first transmitted to the side plate through a combination of four rivets and then transferred to the opposite stiffener through the rivet group on the opposite side. Therefore, the pressure exerted by the rivet group on the hole wall of the aluminum alloy plate becomes a critical factor that leads to connection failure.

Figure 35 illustrates the direction of hole wall pressure exerted by the rivet group on the aluminum alloy stiffener under the bending moment. Based on this, the pressure value of the rivets on the hole wall of the aluminum alloy plate can be calculated. Considering the values of bending moment, axial force, and shear force at that section, the maximum hole wall pressure stress exerted by the rivet group on the aluminum alloy plate is estimated to be approximately 203 MPa. For aluminum alloy grade 3004 in H36 condition, the specified non-proportional elongation stress is $\geq$190 MPa. According to the " Aluminum Alloy Structural Design Specification", the strength standard value for local compressive strength is $160 \times 1.3 = 208$ MPa. It can be observed that the theoretically calculated hole wall pressure stress exceeds the proportional limit of the aluminum alloy and approaches the strength standard value. Under the extrusion of the rivet, localized plastic flow occurs around the hole in the aluminum alloy plate which is consistent with the observed failure mode around the rivet hole in Figure 21. Locally, the failure manifests as yielding and bulging of the aluminum alloy plate while at the overall model level, the failure manifests as excessive displacement at the mid-span, rendering the structural form unsuitable for continued load-bearing.

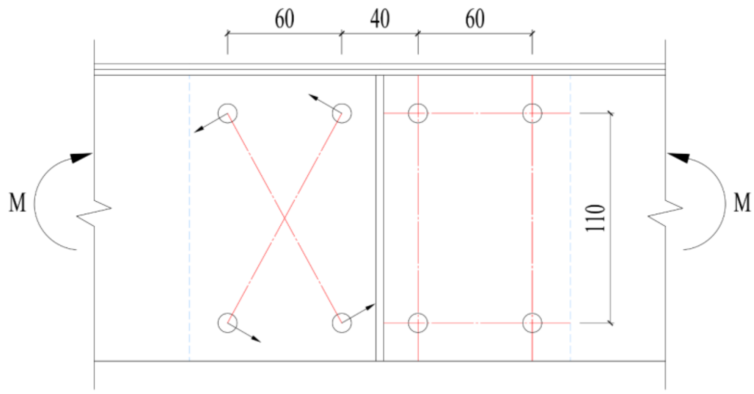

Figure 35. Calculation of stiffener connections.

6. Conclusions

(1) A double-layer aluminum alloy riveted roofing panel suitable for irregular curved roofs was designed. This type of roofing panel features flexible and variable shapes, simple and easy construction, stable and reliable load-bearing capacity, and predictable failure characteristics;

(2) A full-scale model of this roofing panel measuring 3 m×3 m subjected to a stacking load test was carried out. During the test, the displacement pattern of the model resembled that of a simply supported plate, with the upper panel under compression and the lower panel under tension, while the stiffeners acted as the main bending-resistant components. The failure mode of the model involved the stiffeners being sheared by the rivets, resulting in significant vertical displacement and exhibiting ductile failure. Throughout the test, neither the upper nor the lower aluminum alloy panels entered the plastic range, indicating sufficient structural safety redundancy;

(3) Numerical simulations were conducted for both single-layer and double-layer panel models based on the stacking load test. The results showed a good agreement between the double-layer panel model and the experimental data. When compared to each other, the double-layer panel model exhibited higher load-bearing capacity and vertical stiffness, with a more uniform stiffness in both directions and better bending resistance performance. Based on the results of numerical simulations, the load-carrying characteristics of the roof panel were analyzed. It was found that the lower side of the panel mainly relies on transverse stiffening ribs to resist bending moments. The stainless steel bars effectively restrain the displacement of the transverse stiffening ribs, preventing local buckling and ensuring a more uniform bending stiffness in both directions of the panel. These conclusions can provide a reference for the design of similar stiffened roof panels.

(4) The theoretical analysis and calculation of the model's ultimate load-bearing capacity were performed using the process of load distribution on the panel, beam assumption, internal force calculation of the cross-section, and connection stress calculation. The stress around the rivet hole obtained from the theoretical analysis matched well with the experimental results and the predicted failure mode also aligned with the test results. The results indicated that the weak points of the structure were in the rivet connection areas of the stiffeners and that the load-bearing capacity could be improved by optimizing the rivet combination or strengthening the construction of the

connecting plates. In theoretical calculations, the classification of panel hinge regions and the approximations of load values for different types of panels were proposed. The theory of vertical support influence area was applied in the overall analysis of the panels. These calculation methods are not only applicable to the aluminum alloy stiffened roof panels studied in this paper but also have reference values for estimating other large-span stiffened panel problems.

Author Contributions: Conceptualization, Q.Z. and X.L.; methodology, S.Z. and H.G.; software, L.Y. and Y.Y; validation, L.Y., X.L. and Y.Y.; formal analysis, L.Y.; investigation, X.L.; resources, X.L. and S.Z.; data curation, Y.Y.; writing—original draft preparation, Y.Y.; writing—review and editing, Q.Z.; visualization, Y.Y.; supervision, S.Z. and H.G.; project administration, Q.Z. and X.L; funding acquisition, Q.Z. All authors have read and agreed to the published version of the manuscript.

Funding: This research was funded by the National Natural Science Foundation of China, grant number 51738009.

Data Availability Statement: The data presented in this study are available on request from the corresponding author. The data are not publicly available due to the confidentiality agreement between the company and the university.

Conflicts of Interest: The authors declare no conflict of interest. The funders had no role in the design of the study; in the collection, analyses, or interpretation of data; in the writing of the manuscript; or in the decision to publish the results.

References

1. Kissell, J.; Ferry, R. *Aluminum Structures: A Guide to Their Specifications and Design*; John Wiley & Sons: Hoboken, NJ, USA, 2002.
2. Yang, L.; Wei, S.; Zhang, Q. Aluminum reticulated spatial structures: State of the art and key issues. *J. Build. Struct.* **2013**, *34*, 1–19+60. [CrossRef]
3. Zhang, Q. Applications Researches and Developments of Aluminum Alloy Structures in China. *Constr. Technol.* **2018**, *47*, 13–17+25.
4. Shen, Z.; Guo, X.; Li, Y. State-of-arts of research on aluminum alloy structures. *J. Build. Struct.* **2007**, *6*, 100–109. [CrossRef]
5. *GB/T 50429-2007*; Aluminum Alloy Structural Design Specification. China Planning Press: Beijing, China, 2007.
6. Yuan, L.; Zhang, Q.; Luo, X.; Ouyang, Y.; Yin, J. Shear resistance of aluminum alloy extruded H-Section beams. *Thin-Walled Struct.* **2021**, *159*, 107219. [CrossRef]
7. Yuan, L.; Zhang, Q.; Ouyang, Y. Experimental investigation and design method of the flexural buckling resistance of high-strength aluminum alloy H-columns. *Structures* **2022**, *35*, 1339–1349. [CrossRef]
8. Yuan, L.; Zhang, Q. Buckling behavior and design of concentrically loaded T-section aluminum alloy columns. *Eng. Struct.* **2022**, *260*, 114221. [CrossRef]
9. Okafor, V. Finite element analysis of a ribbed roofing panel under static flexure. *Eur. J. Eng. Technol. Res.* **2018**, *3*, 15–20. [CrossRef]
10. Avci, O.; Luttrell, L.D.; Mattingly, J.; Easterling, W.S. Diaphragm shear strength and stiffness of aluminum roof panel assemblies. *Thin-Walled Struct.* **2016**, *106*, 51–60. [CrossRef]
11. Wang, M.; Ou, T.; Xin, Z.; Wang, D.; Zhang, Y. Mechanical behavior and fatigue failure analysis of standing seam aluminum alloy roof system under temperature effect. *J. Build. Eng.* **2021**, *44*, 103001. [CrossRef]
12. Alphonso, T.; Barbato, M. Experimental fragility curves for aluminum storm panels subject to windborne debris impact. *J. Wind. Eng. Ind. Aerodyn.* **2014**, *134*, 44–55. [CrossRef]
13. Song, Y.; Yang, L.; Jiang, H. Finite element analysis on deformation characteristics of metal roof panels under negative wind load. In Proceedings of the 2015 Seventh International Conference on Measuring Technology and Mechatronics Automation, Nanchang, China, 13–14 June 2015; pp. 489–491. [CrossRef]
14. Luo, Y.; Liu, Y.; Wang, L.; Guo, X. Loading behaviour and comparison of two connection systems of the aluminum alloy roof structure under wind loads. In *Proceedings of IASS Annual Symposia*; International Association for Shell and Spatial Structures (IASS): Madrid, Spain, 2014; Volume 19, pp. 1–7.
15. El Mays, A.; Ammar, R.; Hawa, M.; Akroush, M.A.; Hachem, F.; Khaled, M.; Ramadan, M. Improving photovoltaic panel using finned plate of aluminum. *Energy Procedia* **2017**, *119*, 812–817. [CrossRef]
16. Hijazi, A.; Al-Dahidi, S.; Altarazi, S. Residual strength prediction of aluminum panels with multiple site damage using artificial neural networks. *Materials* **2020**, *13*, 5216. [CrossRef] [PubMed]
17. Brando, G.; Matteis, G. Design of low strength-high hardening metal multi-stiffened shear plates. *Eng. Struct.* **2014**, *60*, 2–10. [CrossRef]

18. Paik, J.K.; van der Veen, S.; Duran, A.; Collette, M. Ultimate compressive strength design methods of aluminum welded stiffened panel structures for aerospace, marine and land-based applications: A benchmark study. *Thin-Walled Struct.* **2005**, *43*, 1550–1566. [CrossRef]
19. Paik, K. Empirical formulations for predicting the ultimate compressive strength of welded aluminum stiffened panels. *Thin-Walled Struct.* **2007**, *45*, 171–184. [CrossRef]
20. Zha, Y.; Moan, T. Experimental and numerical prediction of collapse of flatbar stiffeners in aluminum panels. *J. Struct. Eng.* **2003**, *129*, 160–168. [CrossRef]
21. Li, C.; Ren, H.; Zhu, Z.; Soares, C.G. FEM analysis of the ultimate strength of aluminum stiffened panels with fixed and floating transverse frames. International Conference on Offshore Mechanics and Arctic Engineering. *Am. Soc. Mech. Eng.* **2015**, *56499*, V003T02A101. [CrossRef]
22. Paik, J.K.; Kim, B.J.; Sohn, J.M.; Kim, S.H.; Jeong, J.M.; Park, J.S. On buckling collapse of a fusion-welded aluminum-stiffened plate structure: An experimental and numerical study. *J. Offshore Mech. Arct. Eng.* **2012**, *134*, 021402. [CrossRef]
23. De Luca, A.; Perfetto, D.; Lamanna, G.; Aversano, A.; Caputo, F. Numerical investigation on guided waves dispersion and scattering phenomena in stiffened panels. *Materials* **2021**, *15*, 74. [CrossRef]
24. Zhao, C.; Zheng, W.; Ma, J.; Zhao, Y. The lateral compressive buckling performance of aluminum honeycomb panels for long-span hollow core roofs. *Materials* **2016**, *9*, 444. [CrossRef]
25. Tran, K.L.; Douthe, C.; Sab, K.; Dallot, J.; Davaine, L. A preliminary design formula for the strength of stiffened curved panels by design of experiment method. *Thin-Walled Struct.* **2014**, *79*, 129–137. [CrossRef]
26. Ljubinković, F.; Martins, J.P.; Gervásio, H.; da Silva, L.S.; Leitão, C. Experimental and numerical investigation on cylindrically curved steel panels under uniform compression. *Thin-Walled Struct.* **2020**, *149*, 106527. [CrossRef]
27. Piculin, S.; Može, P. Stability behaviour of stiffened curved plates subjected to pure compression. *Thin-Walled Struct.* **2021**, *159*, 107313. [CrossRef]
28. Tran, K.L.; Douthe, C.; Sab, K.; Dallot, J.; Davaine, L. Buckling of stiffened curved panels under uniform axial compression. *J. Constr. Steel Res.* **2014**, *103*, 140–147. [CrossRef]